This is the accepted version of the publication.

This article may be downloaded for personal use only. Any other use requires prior permission of the author and AIP Publishing. This article appeared in Yuan Ma, Yuan-Heng Zhang, Huan-Feng Duan; Three-dimensional flow structures through submerged vegetation patches with uniform and non-uniform stem spacing in an open channel. Physics of Fluids 1 July 2025; 37 (7): 075152 and may be found at https://doi.org/10.1063/5.0271265.

Three-dimensional flow structures through submerged vegetation patches with uniform and non-uniform stem spacing in an open channel

3

1

2

Yuan Ma (马原)¹, Yuan-Heng Zhang (张远恒)¹ and Huan-Feng Duan (段焕丰)^{1,2,*}

56

¹ Department of Civil and Environmental Engineering, The Hong Kong Polytechnic University, Hong Kong SAR, PR China

7 8 9

² Research Institute for Land and Space, The Hong Kong Polytechnic University, Hong Kong SAR, PR China

101112

* Corresponding author

1314

15

1617

18

19 20

21

22

23

24

2526

27

28 29

3031

32

33

34

35

ABSTRACT

This study uses Large Eddy Simulation (LES) combined with the Lattice Boltzmann Method (LBM) to analyze the three-dimensional flow structures through and around submerged finite vegetation patches in an open channel. Vegetation patches, modeled as arrays of circular stems arranged in alignment with varying streamwise and spanwise gaps, are distributed using three schemes: increasing gap, uniform gap, and decreasing gap along channel. The findings reveal that increasing stem density results in smaller wake regions and a shift from large, organized coherent structures to smaller, more numerous and chaotic eddies. When both the streamwise and spanwise gaps are relatively small, the patch acts as a single stem with a complete horseshoe vortex and no detached vortices within the patch. On one hand, when the streamwise gap increases under relatively small spanwise gap situation, the shear layers appear with reducing vortex shedding frequency and drag coefficient and allowing lateral fluid passage. On the other hand, as the spanwise gap also increases, it weakens the interactions between vortices generated from the adjacent stems, forming distinct horseshoe vortices and reducing drag coefficient. Furthermore, for fixed vegetation patch dimensions, adjusting stem distribution along the channel alters flow structures by modifying wake length and vortex shedding patterns, with the drag coefficient decreasing from the increasing gap scheme (denser upstream, Cd highest), to uniform gap scheme (moderate Cd), and to the decreasing gap scheme (less dense upstream, Cd lowest), reflecting reduced flow resistance with upstream sparsity. Based on the results and findings of this study, lower upstream vegetation density is recommended for achieving reduced drag.

363738

Keywords: open channel; submerged vegetation; flow structure; drag force; Large Eddy Simulation (LES)

40 41

39

43 1 Introduction

44

45

46

47

48

49

5051

52

53

54

55

56

57

58

59

60

61

62 63

64

65

6667

68

69

70

71

72

73

74

75

76

77

78

79

80

81

82

83

Analyzing the role of aquatic vegetation in environmental flows from a fluid dynamics perspective reveals their impact on flow characteristics and hydrodynamic processes (Nepf et al., 2012; Zhang et al., 2020; Nakayama et al., 2020). This deepens our understanding of aquatic ecosystems and provides essential scientific foundations for water resource management, ecological protection, and environmental restoration.

In order to provide a comprehensive background, it is necessary to consider the physical mechanisms of flow around and within vegetation. Nepf et al. (2012) reviewed the mean and turbulent flows as well as mass transport in the presence of aquatic vegetation, emphasizing the differences between emergent and submerged canopies and the role of canopy-scale eddies in controlling turbulent exchanges. Edwards et al. (1999) proposed a conceptual model for the dynamics of vegetation on large Alpine river gravel bars, providing insights into the initial successional stages within active river zones.

In rivers, vegetation distribution can be categorized into two types: riparian (Wang et al., 2021) and mid-channel (Yagci et al., 2022). From a fluid dynamics perspective, riparian vegetation exhibits the following characteristics: it absorbs and filters pollutants from surface runoff through its root systems, reducing the pollution load entering the river and acting as a crucial buffer zone. Moreover, it stabilizes the riverbank soil, preventing bank erosion, reducing bank collapse and soil loss, and thus maintaining the stability of the river morphology (Del et al., 2021). Li et al. (2022, 2023) performed an experimental study to analyze the flow characteristics around continuous vegetation patches of varying densities along riverbanks. The study revealed that heterogeneity in vegetation density enhances momentum exchange at the interface, promoting stress-driven infiltration into sparse ($\Phi = 0.05$) vegetation patches while inhibiting it into dense ($\Phi = 0.1$) vegetation patches. Building on this, Liu et al. (2024) carried out numerical studies to further investigate the impact of sparse and dense vegetation patches on turbulence characteristics. Their research demonstrated that the influence of heterogeneous vegetation increases with the density difference between sparse and dense patches, although its effect is generally confined to within 10% of the vegetation patch width. Liu et al. (2022) conducted a three-dimensional numerical study on the fluid dynamics of discontinuously distributed riparian vegetation in open channels using Large Eddy Simulation (LES) methods, approximating the vegetation as a porous medium. Their research indicates that, in addition to vegetation density, the aspect ratio significantly impacts the recirculation patterns, turbulence intensity, turbulent kinetic energy distribution, and momentum transfer efficiency within the vegetated side cavities. Zhang et al. (2022) utilized the Reynolds Stress Model (RSM) to perform a numerical study on the three-dimensional flow around longitudinally discontinuous riparian vegetation patches. Their findings showed that the turbulent kinetic energy in the vegetated zones is significantly higher than in non-vegetated areas. In non-submerged conditions, the turbulence intensity in the patch region is

considerably greater than in the gaps between patches, while in submerged conditions, the turbulent kinetic energy in the vegetated zone increases with the longitudinal length of the patches. Fu et al. (2021) demonstrated that staggered arrangements of vegetation patches along riverbanks could reduce the adjustment zone upstream of the vegetation patches. Within the same side vegetation, the turbulence generated by leading and trailing vegetation patches can overlap, increasing the turbulence intensity produced by the trailing vegetation. Similarly, the trailing vegetation can attenuate the wake turbulence of the leading vegetation patches, thereby limiting their turbulence intensity.

84

85

86

87

88

89 90

91

92 93

94 95

96

97

98

99

100

101

102

103104

105

106

107

108

109

110

111

112

113

114115

116

117

118

119

120

121

122

123124

125

After sandbars form in a river channel, vegetation can grow on them, transforming the sandbars into islands. The presence of vegetation on the sandbar structure complicates the understanding of the hydrological system (Nandi et al., 2024). Midchannel vegetation has the following characteristics: it directly affects water flow velocity and flow patterns by increasing flow resistance, thereby reducing flow speed and diminishing the erosive and scouring forces of the water. Furthermore, mid-channel vegetation traps and filters suspended particles through its roots and stem-leaf structures, promoting sediment deposition and improving water clarity. Additionally, it provides habitat, shelter, and food sources for aquatic organisms, enhancing biodiversity. By altering local flow characteristics and turbulence structures, midchannel vegetation influences material and energy transfer processes, further optimizing the function and health of aquatic ecosystems. Yamasaki et al. (2019) investigated the evolution of vegetation patches in the central region of a river channel. The fastest expansion of the vegetation area occurred during the initial simulation steps when the flow obstruction caused by the vegetation was minimal. Higher velocity thresholds resulted in faster initial growth and higher final vegetation coverage. The patches evolved into one or several elongated islands extending along the watercourse. Yu et al. (2021) conducted an experimental study on vegetation patches located in the center of a river. The vegetation patches were rectangular with rounded corners. As the patches became denser or longer, the stable wake region shortened, and the observed vortices were located closer to the downstream edge of the patch. When the flow blockage reached its maximum limit, Kármán vortices were observed directly behind the vegetation patch. Zhang et al. (2023) designed an experiment to study the environmental flow around mid-channel vegetation. The study confirmed the critical role of the vegetation patch aspect ratio. At low vegetation density, increasing the aspect ratio can generate relatively high velocity gradients in the wake region, thereby promoting the formation of wake vortices. Additionally, Kelvin-Helmholtz vortices are triggered along the lateral edges of the patch, increasing the velocity within the patch and contributing to the generation of wake vortices.

Although previous studies have provided valuable insights, the spatiotemporal features of vegetated patches with varying densities, as well as their interactions with fluid dynamics and turbulent fields, still require further investigation to achieve a full comprehension. Notably, vegetation patches distributed periodically along river channels form vegetated ribbons, which exert an exceptionally significant influence on

riverbed flow structures. However, corresponding research in this area remains insufficient. This study primarily investigates the effects of vegetation patch spacing in both the streamwise and spanwise directions.

This study aims to fill the existing research gaps by analyzing the impact of different stem spacings and distribution schemes on the flow structure in open channel flows. Specifically, we focus on three representative distribution schemes—uniform (B2), gap-increasing (B2I), and gap-decreasing (B2D)—to evaluate the effects of streamwise stem spacing on flow dynamics. In natural river systems, vegetation often appears in the form of limited patches with varying densities and arrangements. Understanding how these factors affect flow dynamics can provide a basis for designing optimal vegetation arrangements in bank management, such as controlling erosion, promoting sediment deposition, or creating ecological habitats. The selection of regular arrangements (such as increasing gaps, uniform gaps, and reducing gaps) is to simulate idealized scenarios for easy parameterization and comparison, providing a foundation for understanding more complex natural arrangements.

The paper is organized as follows: Section 2 details the computational model and boundary conditions. Section 3 introduces the numerical method and validation of the present solver. Section 4 analyzes the obtained results. Section 5 summarizes the findings.

2 Model

There are two common approaches to simulate rigid vegetation. The first approach treats a vegetation patch as a porous medium and utilizes the porosity of porous media to represent vegetation density, which leads to a smaller mesh size and relatively shorter computation time (<u>Liu et al., 2022</u>). However, this method cannot accurately analyze the internal flow structures within the vegetation patch. In contrast, the second approach meticulously considers every stem in the vegetation patch, providing a more realistic representation of flow structures, and it can also examine the influence of stem arrangement on fluid dynamics (<u>Liu et al., 2021</u>). Hence, the current study is suitable for employing the second method.

To examine the influence of stem arrangement on fluid dynamics within and around the patch, the submerged vegetation patch is simulated by circular cylinder (<u>Chang et al., 2015</u>). As shown in Fig. 1, X, Y, and Z of the coordinate system correspond to the streamwise, vertical, and lateral directions, respectively. The main computational domain was $0.6m \times 0.1m \times 0.5m$ in X-, Y-, Z- direction, respectively. The origin of the coordinate system is located at the center of the first row of vegetation, with the bottom wall of the channel defined at Y = 0.

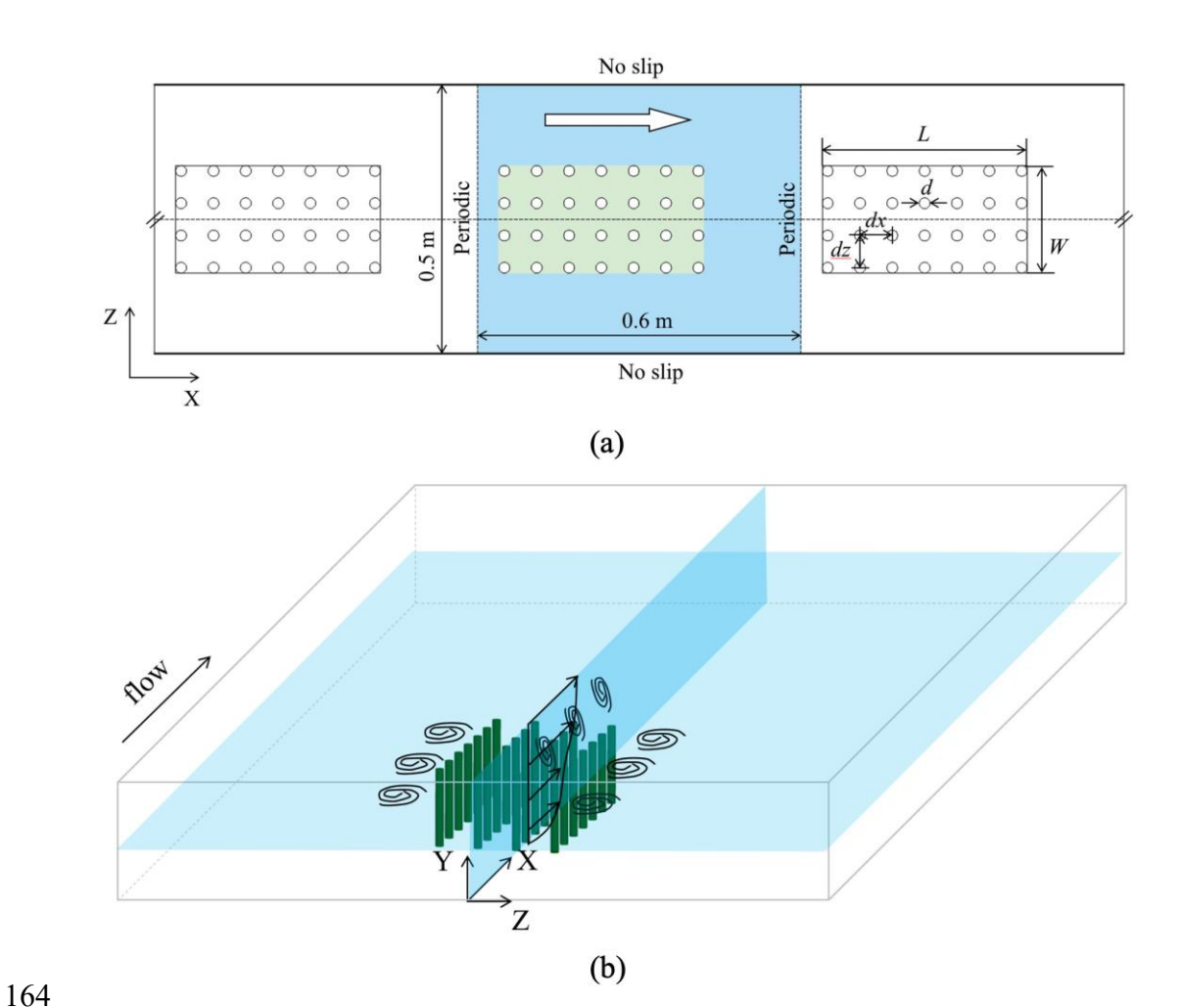


Fig. 1 (a) Top view of the computational domain containing dimensions and boundary conditions. (b) A three-dimensional view of the rectangular vegetated patch contained in the computational domain.

Each submerged vegetation patch was composed of rigid stems with a diameter d=0.0064m (Waterman et al., 2024), and a height of h=0.06m. The stem diameter d=0.0064m was selected based on typical sizes of aquatic vegetation, such as reeds or cattails, observed in rivers and wetlands, with diameters ranging from a few millimeters to over a centimeter. This value represents a medium-sized stem, facilitating the study of its effects on flow resistance. The stems were arranged in an alignment. The vegetation patch consisted of N=28 stems arranged in a 4×7 grid. Three distribution schemes were investigated: uniform (B2), increasing gap (B2I), and decreasing gap (B2D), representing key variations in stem spacing to examine their effects on flow dynamics. The stem spacings are normalized by the diameter of the stem, referred to as the streamwise spacing ($\delta x=dx/d$) and spanwise spacing ($\delta z=dz/d$), respectively. By varying δx and δz between the cylinders, the patch-averaged solid volume fraction ($\Phi=\frac{N\pi d^2}{4LW}$), as well as the width (W) and length (L) of the vegetation patch, are adjusted accordingly. The geometric parameters for each simulation cases are presented in Table

1. The flow velocity was fixed at 0.08 m/s. The water depth is H = 0.1m, leading to a submergence ratio H/h = 1.67. The channel Reynolds number is $Re = U_{\infty}H/\nu = 7986$.

Table 1 Characterization of the principal geometric and flow parameters

Case	L(m)	W (m)	δx	δz	Φ	uniformity
A1	0.06	0.03	1.5625	1.5625	0.5	uniform
A2	0.12	0.03	3.125	1.5625	0.25	uniform
A3	0.18	0.03	4.6875	1.5625	0.167	uniform
B1	0.06	0.06	1.5625	3.125	0.25	uniform
B2	0.12	0.06	3.125	3.125	0.125	uniform
В3	0.18	0.06	4.6875	3.125	0.083	uniform
C1	0.06	0.09	1.5625	4.6875	0.167	uniform
C2	0.12	0.09	3.125	4.6875	0.083	uniform
C3	0.18	0.09	4.6875	4.6875	0.066	uniform
B2I	0.12	0.06	3.125	3.125	0.125	increasing
B2D	0.12	0.06	3.125	3.125	0.125	decreasing

Fig. 2 presents the distribution details of three vegetation distribution schemes: uniform, decreasing, and increasing. For the non-uniform distribution schemes, the vegetation patches are divided into three blocks: block 1, block 2, and block 3. Within each block, the stem spacing is constant, with distances of dx_1 , dx_2 and dx_3 , respectively. For the decreasing gap arrangement, the spacing between consecutive stems follows the relation dx_{i+1} - dx_i =-0.01m. Conversely, for the increasing gap arrangement, the spacing between consecutive stems follows dx_{i+1} - dx_i =0.01 m.

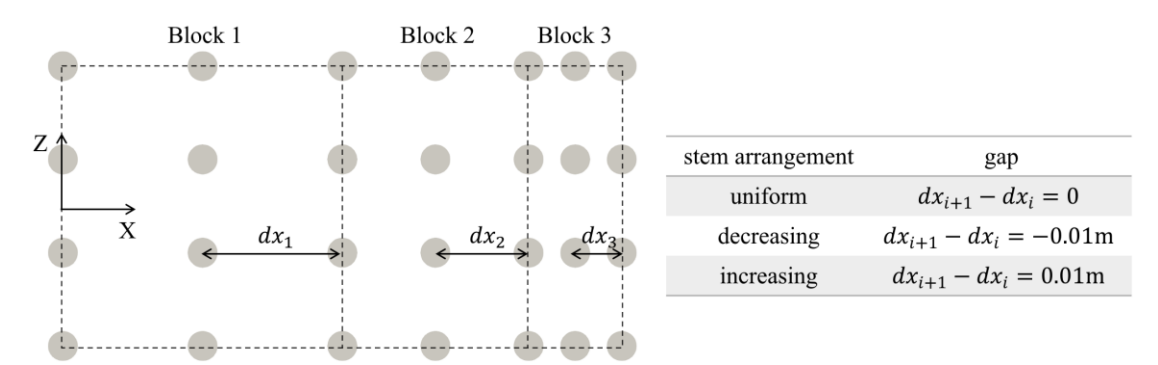


Fig. 2 Stem distribution map of three distribution schemes within the vegetation patch.

One vegetation patch was included in the computational domain (Fig 1b), and periodic streamwise flow conditions were adopted. In other words, the channel simulated in the present work is infinitely long, and the flow is fully developed. Periodic boundary conditions were applied in the streamwise direction to simulate an infinitely long channel, ensuring fully developed flow while isolating the effects of stem spacing. Future studies may explore configurations involving multiple patches or non-periodic

boundary conditions to further investigate spatial heterogeneity.

Non-slip boundary conditions were imposed to sidewalls and bottom of the channel, and the stem surfaces. In the current simulations, the free surface is modeled as a frictionless rigid lid, given that the Froude number $Fr = U_{\infty}/(gH)^{0.5} = 0.081$. Generally, the rigid-lid assumption is highly effective when Fr < 0.5 and has been widely adopted in previous studies of flow around bluff bodies. (Etminan et al., 2017; Liu et al., 2021)

In the subsequent sections of this document, the units of length, time, and velocity are meters (m), seconds (s), and meters per second (m/s), respectively. For brevity, these units will not be reiterated throughout the text. A structured grid was employed in the current simulation, with a maximum mesh size of approximately 0.003m. Mesh refinement was performed in appropriate locations such as the river wall, the wall of vegetation and the vicinity of the vegetation.

218219

220

221

222

223

206

207

208

209

210

211212

213

214215

216

217

3 Numerical method and validation

The lattice Boltzmann method is a dimensionless model, where all quantities are formulated in the dimensionless lattice Boltzmann units. In the present work, the lattice Boltzmann 3D Large Eddy Simulation (LES) code advances the governing continuity and momentum equations over time.

224225

226

3.1. The Lattice Boltzmann Method (LBM)

The Lattice Boltzmann Method (LBM) in this study adheres to the standard formulation described in <u>Chen and Doolen (1998)</u> and <u>Guo and Shu (2013)</u>, employing the D3Q19 lattice model with the BGK collision operator. No modifications were made to this established approach. The lattice Boltzmann equation is:

231
$$f_i(\mathbf{x} + e_i \delta_t, t + \delta_t) - f_i(\mathbf{x}, t) = -\frac{\delta_t}{\tau} [f_i(\mathbf{x}, t) - f_i^{eq}(\mathbf{x}, t)]$$
 (1)

- where f_i represents the density distribution function, f_i^{eq} denotes the equilibrium
- 233 distribution function and τ is the relaxation time attributed to the fluid particle
- collisions. In LBM simulations, the relaxation time is related to the viscosity of the fluid.
- e_i is the discrete velocity in the ith direction. In the D3Q19 model, 19 different
- directions are defined for simulations in three dimensions, which is:

237
$$e_{i} = \begin{cases} (\pm 1,0,0)c, (0,\pm 1,0)c, (0,0,\pm 1)c & for \ i = 1,\dots,6\\ (\pm 1,\pm 1,0)c, (\pm 1,0,\pm 1)c, (0,\pm 1,\pm 1)c & for \ i = 7,\dots,18\\ (0,0,0)c & for \ i = 0 \end{cases}$$
 (2)

238 The equilibrium distribution function for the incompressible flow is:

239
$$f_i^{eq} = w_i \rho \left[1 + \frac{3e_i \cdot u}{c^2} + \frac{9(e_i \cdot u)^2}{2c^4} - \frac{3u^2}{2c^2} \right]$$
 (3)

240

241 The weighting factors w_i for the D3Q19 model is:

242
$$w_i = \begin{cases} 1/18 & for \ i = 1, ..., 6 \\ 1/36 & for \ i = 7, ..., 18 \\ 1/3 & for \ i = 0 \end{cases}$$
 (4)

243 The kinematic viscosity can be calculated by:

244
$$v = \frac{1}{3}(\tau - \frac{1}{2})c^2\delta_t$$
 (5)

- The macro-scale quantities for the density, ρ , and momentum, ρu , can be computed
- from the distribution function, and the discrete velocities. This can be achieved through
- the following calculations:

$$248 \rho(\mathbf{x}, t) = \sum_{i} f_i(\mathbf{x}, t) (6)$$

$$249 \quad \rho u(\mathbf{x}, t) = \sum_{i} e_{i} f_{i}(\mathbf{x}, t) \tag{7}$$

250

251 3.2. Large eddy simulation for lattice Boltzmann equation

- 252 The Large Eddy Simulation (LES) extension of the Lattice Boltzmann Equation
- 253 (LBE) involves incorporating sub-grid scale (SGS) models into the LBM framework to
- account for the effects of smaller turbulent eddies that cannot be resolved directly. This
- approach allows for more accurate simulations of turbulent flows by filtering out the
- small-scale fluctuations while retaining the larger, more significant structures in the
- 257 flow field (Malaspinas et al., 2011).
- 258 The filtered form of the LBE for LES is modeled as:

259
$$\widetilde{f}_{l}(x + e_{l}\delta_{t}, t + \delta_{t}) - \widetilde{f}_{l}(x, t) = -\frac{\delta_{t}}{\tau_{t}} \left(\widetilde{f}_{l}(x, t) - \widetilde{f}_{l}^{eq}(x, t) \right)$$
 (8)

- 260 The effect of the unresolved scale motion is modeled through an effective collision
- relaxation time scale τ_t . Thus, in the LBE, the total LES effective relaxation time is
- 262 $\tau_* = \tau_0 + \tau_t$.

263

264 Accordingly, the total viscosity v^* can be denoted as:

$$265 v^* = v_0 + v_t (9)$$

- In the present work, the subgrid closure is achieved using the Smagorinsky model
- 267 (Smagorinsky, 1963). This model is a widely used approach in LES to account for the
- 268 effects of smaller, unresolved turbulent eddies. The Smagorinsky model defines the
- 269 subgrid-scale eddy viscosity v_t as:

$$270 \qquad \mathbf{v}_t = \left(C_s \, \Delta_x\right)^2 |S| \tag{10}$$

- where
- C_s is the Smagorinsky constant.
- 273 Δ_x is the filter width, typically related to the grid size.

|S| is the magnitude of the strain rate tensor, given by:

$$|S| = \sqrt{2S_{ij}S_{ij}} \tag{11}$$

276 and the strain rate tensor S_{ij} is defined as:

$$S_{ij} = \frac{1}{2} \left(\frac{\partial u_i}{\partial x_j} + \frac{\partial u_j}{\partial x_i} \right) \tag{12}$$

278279

280

281282

283

284

285286

287

288

289290

291

It is important to note that there are significant differences in the implications of the Smagorinsky closure in LBE-LES and NS-LES. In NS-LES, the subgrid-scale stress immediately responds to the current filtered strain rate without any time lag, implying an instantaneous effect. This means that the subgrid-scale stress is in equilibrium with the instantaneous local strain rate. In contrast, in LBE-LES, the subgrid-scale stress reaches equilibrium through a relaxation process, introducing a time lag effect and exhibiting spatiotemporal memory. Therefore, the subgrid-scale stress in LBE-LES does not immediately balance with the filtered strain rate. Instead, the stress relaxes towards the value determined by the filtered strain rate at a relaxation rate dictated by the current eddy viscosity. Consequently, the LBE-LES formulation may result in more pronounced spatiotemporal memory effects. In NS-LES, the influence of the eddy viscosity is instantaneous, and non-hydrodynamic variables are completely neglected. Preliminary studies using the LBE-LES method have demonstrated favorable outcomes (Coratger et al., 2021; Siodlaczek et al., 2021; Wu et al., 2024).

292293

294

295

296

297

298

299300

301

302

303

304

305

306307

308

309310

311

3.3. Validation and grid independence

To validate the accuracy of the numerical method employed in this study, a comparison was made between the numerical simulation results and previous experimental data by Zong and Nepf (2011), including the staggered stem arrangement. The validation results showed strong agreement with the experimental data, confirming the model's accuracy. It should be noted that the primary cases in this study (B2, B2I, B2D) employ rectilinear arrangements to systematically investigate the effects of stem spacing variations. The experimental setup consisted of a 16-meter-long, 1.2-meterwide flume, with one side containing model vegetation arranged in a staggered scheme of cylindrical structures, each 6 mm in diameter. The vegetated zone spanned 10 meters in length and 0.4 meters in width. In the current comparative study, we performed simulations for the case of sparse vegetation patches ($\Phi = 0.02$) under flow conditions characterized by a medium velocity (9 cm/s). Further information can be found in Zong and Nepf's work. Considering the extended length of the vegetated region, a periodic boundary condition was applied in our simulations to represent the vegetation patches. Each stem within the vegetation patch was modeled as a cylinder, consistent with the experimental setup. Boundary conditions mirrored those of the experimental configuration, except for the inflow and outflow boundaries.

As seen in Fig. 3, the numerical results closely match the experimental data in most regions, particularly in areas where the velocity increases and reaches its peak, demonstrating the ability of the numerical method to accurately capture the velocity variations around the vegetation. Within the patch, the numerical simulation shows small oscillations in velocity. These oscillations arise from the flow behavior within the vegetation zone: velocity is lower near the vegetation elements and higher in areas farther from the vegetation, leading to periodic velocity fluctuations. Overall, the numerical method used in this study successfully reproduces the velocity distribution of flow through vegetation in an open channel. The comparison with experimental data confirms the validity of the method and provides a reliable numerical foundation for investigating more complex flow problems involving vegetation.

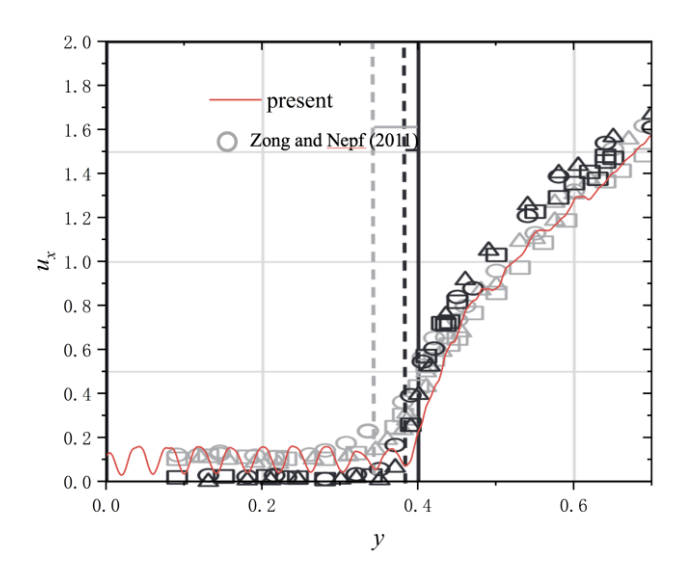


Fig. 3 Comparison of the simulated streamwise velocity profile (red curve) with experimental data from Zong and Nepf (2011). The gray circles represent the experimental results for the condition replicated in our simulation, while other symbols (black circles, squares, triangles) denote additional experimental configurations from the original study. The x-axis represents the streamwise direction, and the y-axis denotes the spanwise distance from the vegetation centerline.

The computational grid was designed to satisfy LES requirements, with a minimum grid size of $\Delta x = 0.0004$ m (approximately d/16 where d = 0.0064m is the stem diameter) near the stems and channel bed, enabling resolution of key turbulent structures. The near-wall first-layer thickness is $\Delta y = 0.0001$ m, corresponding to $\Delta y^+ \approx 1$, ensuring accurate simulation of the viscous sublayer. Grid independence tests confirmed the convergence of the results. Fig. 4 represents a mesh independence study, which is an essential process in CFD to ensure that the results are not influenced by the mesh resolution. The x-axis shows the number of grid points, starting from a coarse mesh on the left to a very fine mesh on the right. The y-axis represents the drag coefficient (Cd). With a coarse mesh, the drag coefficient is relatively high, around 0.45,

suggesting that the coarse mesh does not sufficiently capture the flow details, leading to an overestimated Cd. As the mesh is refined to a medium mesh, the Cd decreases significantly, indicating improved accuracy in the simulation as more grid points are used. When the mesh is further refined to a fine and very fine mesh, the drag coefficient stabilizes at around 0.25. This indicates that beyond a certain number of grid points, the results no longer change significantly, meaning that the solution has become mesh independent. The graph demonstrates that for this simulation, a fine mesh (around 4×10^7) is sufficient to achieve accurate results. Further refinement, such as with a very fine mesh, only results in marginal changes to the drag coefficient, confirming that the solution has converged.

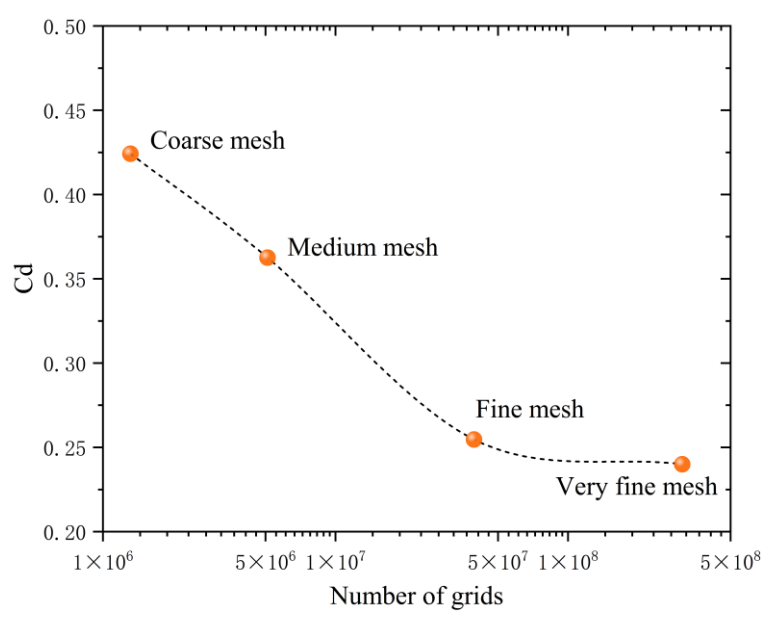


Fig. 4 Mesh independence study showing the variation of drag coefficient with the number of grids.

4 Results and discussion

4.1 Mean flow pattern

Fig. 5 shows the effects of streamwise stem spacing (δx) on time-averaged streamwise velocity (u_x) distribution around the vegetation patch. It is evident that the vegetation exerts a significant shielding effect. In fluid mechanics, the shielding effect refers to the phenomenon in which objects or structures, such as vegetation or obstacles, reduce the force or impact of the flow on downstream elements by obstructing or redirecting the flow around them. Spacing dominates the shielding effect between the stems. The strong shielding effect under small δx limits the downstream flow development, while larger spacings provide more space for the flow to reorganize, leading to an extended wake region after each individual stem and the whole patch. In

the case of $\delta x = 1.5625$, the small stem spacing causes the flow to quickly separate after encountering the first stem, forming a relatively short wake region. Due to the dense arrangement of the stems, flow reattachment occurs rapidly in the downstream region. When δx increases to 3.125 and 4.6875, the steady wake zone becomes more widespread behind the stems, and the wake lengthens as well. From the perspective of the XY-plane (Fig. 5(a2-c2)), there is a noticeable velocity difference between the regions directly above and below the vegetation. It can be observed that the flow beneath the vegetation slows down considerably, while the flow above the vegetation accelerates. This indicates that the vegetation exerts a significant blocking effect on the water flow, particularly forming a wake in the downstream region. Due to the deceleration of flow beneath the vegetation, a distinct stratification of the fluid emerges in this area. In summary, different stem spacings affect the flow structure in terms of wake length and flow separation position. Smaller spacings cause stronger interactions between stems, resulting in shorter wake regions, while larger spacings allow for extended wake regions.

Fig. 5 Time-averaged x-direction velocity (u_x) contour plots for stem arrays in an open channel at different stem spacings, $\delta x = 1.5625$ (a1-a2), 3.125 (b1-b2), 4.6875 (c1-c2). The first row shows the velocity distribution in the XZ-plane at Y = h/2 = 0.03m, and the second row shows the distribution in the XY-plane at Z = 0 (channel center).

The spanwise spacing (δz) dominates the lateral interference between stems. The stronger lateral interaction under a small δz leads to a shorter wake region (Fig. 6). As δz increases, the fluid has more space to recover momentum after passing through the stem array, resulting in a considerably longer wake region. Smaller δz (1.5625) limits lateral flow freedom, leading to a shorter wake region and quicker recovery. As a result, the flow reattachment occurs earlier, and the extent of the wake region is suppressed. Conversely, as δz increases to 3.125 and 4.6875, the length of the wake region grows, and the steady wake zone expands. Results from the XY-plane also show that, as Z-direction spacing increases, the area and length of the steady wake zone gradually increase. In summary, smaller δz values suppress momentum recovery and result in shorter wake regions, while larger δz values promote the development of more extensive wake regions.

Fig. 6 Time-averaged x-direction velocity (u_x) contour plots for stem arrays in an open channel at different stem spacings $\delta z = 1.5625$ (a1-a2), 3.125 (b1-b2), 4.6875 (c1-c2). The first row shows the velocity distribution in the XZ-plane at Y = h/2 = 0.03m, and

407 the second row shows the distribution in the XY-plane at Z = 0 (channel center).

Fig. 7 shows the time-averaged distribution of x-direction velocity (u_x) for stem arrays in an open channel at different stem spacings B2I, B2, B2D. The sharp increase in u_x near the free surface reflects the transition from the vegetation layer to the free-stream region. For the B2I configuration, the fluid encounters strong resistance, causing early flow separation and a shorter wake region in the initial region. However, as the spacing increases, the fluid momentum gradually recovers, and the wake region extends significantly downstream. This configuration has potential applications in scenarios where reducing downstream resistance is critical. In the B2 configuration, the stem spacing remains uniform throughout. The flow separation and reattachment points are evenly distributed, and the wake region length remains relatively consistent. The process of momentum loss and recovery is stable across the stem array, resulting in a symmetric flow structure. For the B2D configuration, the stem spacing decreases along the flow direction. The results reveal that the downstream region experiences greater flow disruption, with the wake region extending significantly and momentum recovery becoming more challenging.

Fig. 7 Time-averaged x-direction velocity (u_x) contour plots for stem arrays in an open channel at different stem spacings B2I (a1-a2), B2 (b1-b2), B2D (c1-c2). The first row shows the velocity distribution in the XZ-plane at Y = h/2 = 0.03m, and the second row shows the distribution in the XY-plane at Z = 0 (channel center).

To investigate effects of stem spacing on flow adjustment, the time-averaged nondimensional streamwise velocity u_x along the centerline for different stem spacings $(\delta x = 1.5625, 3.125, 4.6875)$ were compared (Fig. 8). The streamwise velocity (u_x) along the centerline, defined as (Z = 0) (spanwise center) and (Y = h/2 = 0.03m) (midstem height), was analyzed to capture the flow within the vegetation layer. Near the inlet (x < 9.4), velocity drops significantly due to stem obstruction. In this region, the velocity curves for all spacings almost overlap, indicating that the effect of stem streamwise spacing is not yet significant at the initial stage of flow. In the middle region (9.4 < x < 18.8), larger spacings lead to an extended wake region, making the downstream momentum recovery process more complex. The results indicate that although increasing the spacing is generally expected to reduce local resistance, the velocity for $\delta x = 4.6875$ is actually lower than that for $\delta x = 1.5625$ and 3.125, particularly in the downstream region (x > L). In the downstream region, the delayed velocity recovery is particularly evident for the larger spacing ($\delta x = 4.6875$). Although the local turbulence effects are reduced, the wake region extends further, and the reattachment point is delayed, resulting in a slower velocity recovery that is even lower than for smaller spacings. This phenomenon suggests that while larger spacings reduce local turbulence mixing, the extension and complexity of the wake structure prolong the velocity recovery process.

For a narrow lateral spacing ($\delta z = 1.5625$), the rapid drop in velocity indicates earlier and stronger flow separation. As δz increases, the velocity drop is more gradual, indicating that the fluid has more freedom in the z-direction, allowing it to navigate the stem array with reduced flow separation. The velocity recovers more rapidly for the smallest z-direction spacing ($\delta z = 1.5625$), while the recovery is slower for larger spacings ($\delta z = 3.125$ and 4.6875). For the smallest z-direction spacing ($\delta z = 1.5625$), the recovery process is expedited, as a smaller δz corresponds to higher density and narrower patch width, both of which contribute to a faster recovery. Conversely, for larger spacings ($\delta z = 3.125$ and 4.6875), the flow remains more stable. In this case, the reattachment point shifted further downstream, leading to a longer wake region. Although the periodic boundary conditions maintain the cyclic nature of the flow, the larger z-direction spacing allows for smoother flow past the stems with less disturbance, resulting in weaker vortex structures and less efficient momentum transfer.

Fig. 8 Time-averaged streamwise velocity u_x along the centerline for (a) different uniform-distributed streamwise spacings (δx), (b) different uniform-distributed spanwise spacing (δz), and (c) varying spacings with the averaged spacing $\overline{\delta x} = \overline{\delta z} = 3.125$. The shaded regions represent the vegetation zone.

For three different gap configurations (Fig. 8c), velocity decreases similarly along the centerline. In the B2I case, the vegetation density increases along the flow direction. From the velocity profile, it is evident that the velocity fluctuations upstream within the vegetated patch are significantly smaller than those downstream within the patch. In contrast, in the B2D case, the velocity fluctuations are greater upstream within the vegetated patch. Nevertheless, the overall velocity profiles for the three vegetated patches, B2I, B2, and B2D, are nearly identical.

4.2 Instantaneous turbulent field

Fig. 9 shows the vertical vorticity contour plots at the Y = 0.05m and 0.002m planes and the Fast Fourier Transform (FFT) of drag force for different δx values. It is worth noting that the vegetation spacing in the z direction is fixed at δz = 1.5625. At Y = 0.05m, it can be observed that since the width of the three vegetation patches are consistent, the size of steady wake zones they create do not differ significantly in the z direction. Specifically, at δx = 1.5625, the stems are very close to each other, decaying the incoming flow to pass through the gaps between the stems, and the fluid velocity entering the vegetation patch decreases along the flow direction. Due to the close spacing (δx = 1.5625), coherent vortex structures do not form behind individual stems, as the limited space and flow interference from adjacent stems suppress distinct shedding patterns, although vorticity is still shed into the wake. The flow separation on

the lateral sides of the vegetation patch leads to the formation of leading-edge vortices (LEV) (Son et al., 2022). Additionally, a trailing edge vortex forms behind the vegetation patch and sheds in the form of a Kármán vortex street.

When the spacing δx increases to 3.125, the flow within the vegetation patch becomes more complicated. As the fluid passes through the first row of stems, the generated LEVs collide with the second row of stems, creating more fragmented vortices. Indicated by the vorticity, the strength of the vortices behind the second row of stems is significantly weaker than that of the first row. Unlike the scenario with $\delta x = 1.5625$, LEV-like vortices form on both sides of each row of stems. When δx increases to 4.6875, the spacing further increases. The steady wake region behind the vegetation patch continues to shrink. Within the vegetation patch, the fluid channels in the z-direction become more pronounced.

The analyzed plane is at Y = 0.05m, which is close to the top of the stems since the stem height is 0.06m. In contrast, the plane at Y = 0.002m is closer to the lower end of the stems. It is observed that the vorticity intensity significantly decreases near the ground plane. A distinct vorticity pattern is visible only around the first row of stems in the vegetated patch, while the vorticity intensity in the downstream rows is much lower. This reduction, compared to the Y = 0.05m plane, is attributed to the influence of ground friction.

Additionally, a FFT analysis was conducted to examine the vortex shedding frequency. The FFT results reveal the primary frequency of vortex shedding. It can be observed that in all the cases studied, there is a dominant frequency, and this primary frequency decreases as the δx increases. It should be noted that, throughout the paper, identical legends are used for the contour plots of the same physical quantities.

Fig. 9 Vertical vorticity contours in instantaneous fields at Y = 0.05m (left column) and 0.002m (right column) for (a1-a2) δx = 1.5625, (b1-b2) δx = 3.125, (c1-c2) δx = 4.6875, and the fast Fourier transform (a3-c3), at δz = 1.5625 and different δx .

Due to the height of the vegetation being less than the water depth, it is necessary to consider the influence of the free ends of each stem. In fact, the flow over the free ends of finite-height stems is a very important topic, encompassing complex flow structures (Sumner, 2013). Fig. 10 presents the velocity and vorticity contours in the Z = 0 plane. As previously mentioned, when $\delta x = 1.5625$ and $\delta z = 1.5625$, the flow separates at the leading edge of the vegetation patch free end, forming a distinct recirculation zone (white narrow in Fig. 10(a1)) above the top of the vegetation patch. Moreover, the vortices shed from the rear of the top of the vegetation patch are also pronounced. When the spacing increases to 3.125, although the flow near the leading edge of the top of the vegetation patch remains similar, the height of the recirculation zone at the top decreases. This is because the increased distance between the stems reduces the obstructive effect of the free ends on the fluid flow, thereby reducing the

boundary layer thickness. The fluid velocity between the stems increases with the spacing, which naturally reduces the size of the recirculation zone at the top. Additionally, the larger spacing allows the trailing vortex shed from upstream to impact the downstream stems. This is evident in the staggered vortex shedding layer surrounding the top surface of the vegetation patch. The similar situation also occurs when $\delta x = 4.6875$.

538

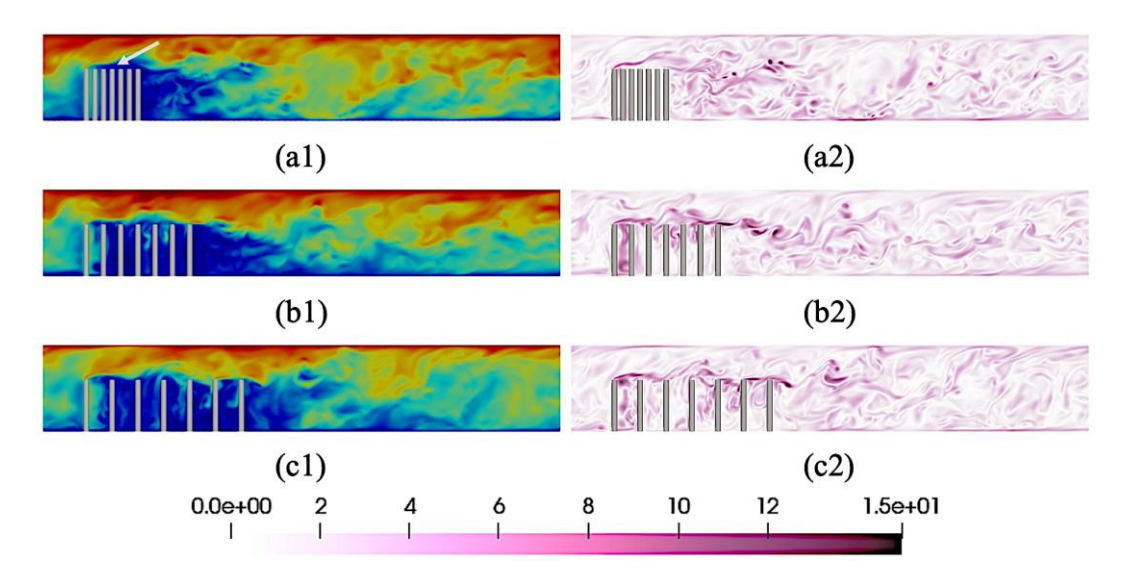
532533

534

535

536

537



539 540

Fig. 10 Velocity (left column) and vorticity (right column) contours in instantaneous fields at Z = 0 plane and $\delta z = 1.5625$ for different δx , (a1-a2) $\delta x = 1.5625$, (b1-b2) $\delta x = 3.125$, (c1-c2) $\delta x = 4.6875$.

542543

544

545

546

547

548

549

550

551

552

553

554

555

556

557558

559

560

541

Fig. 11 shows the coherent structures around the vegetation patch visualized using the Q criterion (Dubief and Delcayre, 2000). The Q criterion is an important method for identifying vortex structures in a flow field. In three-dimensional flows, vortex structures are typically associated with localized rotational motion. The Q criterion $(Q = \frac{1}{2}(\|\Omega\|^2 - \|S\|^2))$ quantifies the dominance of rotation in the flow by comparing the rates of rotation and strain, which are represented by the rotation rate tensor (Ω) and the strain rate tensor (S), respectively. Triggered by the velocity shear between the vegetated region and the free stream regions, several types of vortices are formed: the upstream horseshoe vortex formed at the interface between the vegetation patch and the bottom wall (Frederich et al., 2008), the trailing vortex formed above, on the side edges and at the free ends of the stems, and the Kármán vortex formed behind the stems. The observed formation of horseshoe vortices can be explained by the study of Zong and Nepf (2011), which describes the mechanism of vortex development behind finite porous obstacles. When $\delta x = 1.5625$, the vortices from the first row of the patch almost envelop the second and even the third rows of stems. Due to the small spacing between the stems, the decay of the interior velocity suppresses the generation of stem-scale vortices (Liu and Nepf, 2016). As the spacing in the x-direction increases, the downstream stems are no longer enveloped by the vortices shed from the first row of stems. Instead, they interact with these vortices, leading to more involved vortex formations. Specifically, at $\delta x = 4.6875$, the increased spacing allows the downstream stems to generate shear layers on their surfaces, which then shed vortices downstream.

Fig. 11 Visualization of the coherent structures in an instantaneous flow field using the Q criterion at $\delta z = 3.125$ for different δx , (a) $\delta x = 1.5625$, (b) $\delta x = 3.125$, (c) $\delta x = 4.6875$.

As previously mentioned, increasing the spacing in the x-direction essentially adds transverse channels (Z-direction) within the vegetation patch, thereby enhancing the fluid passing through. This phenomenon is clearly illustrated by the streamlines in Fig. 12. At $\delta x = 1.5625$, only a small portion of the fluid flows outward within the vegetation patch. This fluid enters through the gaps between the first row of stems, where it faces the incoming flow directly, enters the gaps at a relatively high speed, and then flow out from the sides. The flow diversion leads to a reduction in flow velocity. When δx increases, it becomes evident that the vegetation patch interior contains not only fluid entering from the front and exiting from the sides but also fluid flowing in from the sides, which explains why the velocity recovers before the end of the patch when the streamwise spacing increases.

The side view reveals that when $\delta x = 1.5625$ and 3.125, the fluid entering from the front row of the vegetated patch exits from the upper middle section of the patch. However, when $\delta x = 4.6875$, the fluid predominantly exits from the bottom of both sides of the vegetation patch. This is the evidence that when streamwise spacing is small, the flow adjustment is dominated by the vertical flow diversion. In contrast, for $\delta x = 4.6875$, the increased streamwise spacing between the stems enhances the potential for lateral flow within the vegetation.

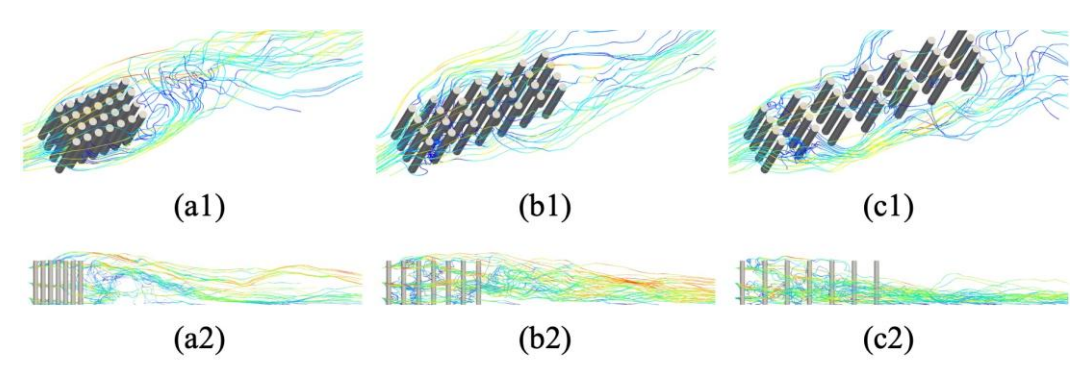


Fig. 12 Streamlines through and around the vegetated patch at $\delta z = 1.5625$ for different δx , (a1-a2) $\delta x = 1.5625$, (b1-b2) $\delta x = 3.125$, (c1-c2) $\delta x = 4.6875$.

Fig. 13 shows the vertical vorticity plots on the Y = 0.05m planes for different δz values. At $\delta z = 1.5625$, no obvious separation flow or vortex shedding is observed. When $\delta z = 3.125$, the flow within the vegetation patch resembles four tandem arrays of

stems. In each array, the shear layer separated from the first stem reattaches to the downstream stem. Because of the small gaps between the stems, no vortex shedding occurs behind the upstream stems, with shedding occurring only behind the last stems. Notably, since δz is not large enough, the shear layers from each stem array interact with those of adjacent arrays. At $\delta z = 4.6875$, the lateral spacing between the stems increases, reducing the interaction between shear layers from different arrays. The frequency analysis demonstrates that the two distinct vegetation patches ($\delta z = 3.125$ and 4.6875) exhibit similar dominant vortex shedding frequencies.

Fig. 13 Vertical vorticity contours in instantaneous fields at Y = 0.05m for (a) $\delta z = 1.5625$, (b) $\delta z = 3.125$, (c) $\delta z = 4.6875$ and the fast Fourier transform planes, at $\delta x = 3.125$ and different δz .

Fig. 14 presents the velocity and vorticity contours on the Z=0 plane. As δz increases, the fluid velocity downstream of the vegetation patch significantly increases. Combining this with Fig. 13, it can be concluded that increasing δz extends the longitudinal size of the steady wake region. Consistent with previous observations in the emergent circular patch (Zong and Nepf 2011), a larger after-patch velocity leads to a larger steady wake region. Compared to the changes in the steady wake region caused by increasing δx (Fig. 9 and Fig. 10), the impact of δz is more pronounced. It is noteworthy that this section is located at Z=0, which is the mid-plane, where stems are symmetrically distributed on both sides, with no stems located on this plane. When $\delta z=1.5625$, the distance between the stems on either side of the mid-plane and the plane is 0.005m. Due to the small spacing, clear vortex shedding can be observed on this plane, indicating the interaction of the stem-scale vortices. However, as δz increases to 3.125 or even 4.6875, the lateral interaction of the interaction of the stem-scale vortices decays. Consequently, the intensity of vortex shedding observed on this plane is lower than that at $\delta z=1.5625$.

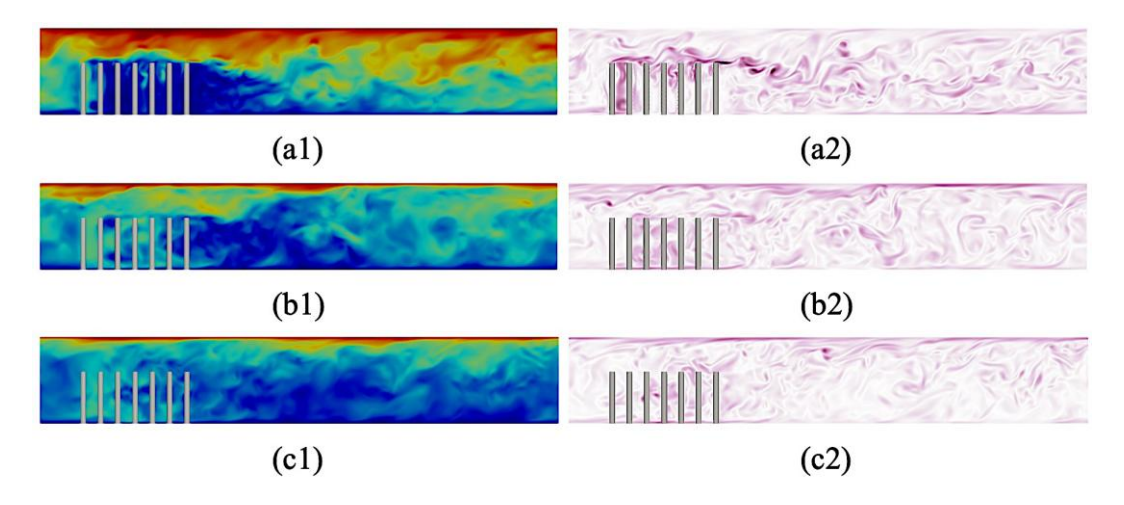


Fig. 14 Velocity (left column) and vorticity (right column) contours in instantaneous

fields at Z = 0 plane and $\delta x = 3.125$ for different δz , (a1-a2) $\delta z = 1.5625$, (b1-b2) $\delta z = 3.125$, (c1-c2) $\delta z = 4.6875$.

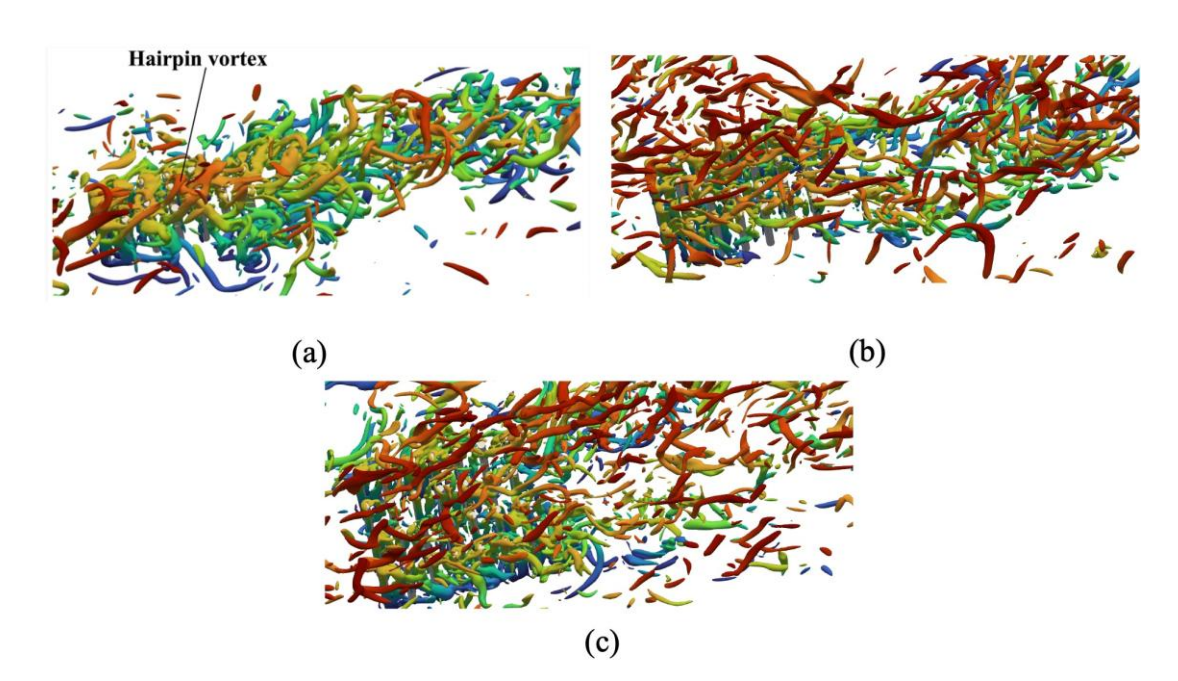


Fig. 15 Visualization of the coherent structures in an instantaneous flow field using the Q criterion at $\delta x = 3.125$ for different δz , (a) $\delta z = 1.5625$, (b) $\delta z = 3.125$, (c) $\delta z = 4.6875$.

Fig. 15 shows the coherent structures in the instantaneous flow field using the Q-criterion for different δz values. When $\delta z = 1.5625$, a horseshoe vortex is present between the vegetated patch and the bottom wall, formed collectively by the closely spaced stems in the first row. As δz increases, the spacing between the stems becomes sufficiently large, resulting in the formation of individual small horseshoe vortices in front of each column of stems. Hairpin vortices marked in Fig. 15, play a crucial role in enhancing turbulent mixing within the vegetation patch. These structures, commonly observed in turbulent boundary layers, facilitate momentum and mass transfer through their rotational motion. In the context of vegetated flows, hairpin vortices contribute to the vertical transport of fluid, which can influence sediment deposition and nutrient distribution in natural river systems, thereby impacting ecological processes.

Fig. 16 illustrates the streamlines within and around the vegetation patch at $\delta x = 3.125$ for different δz values. When $\delta z = 1.5625$, the small spacing in the z-direction causes the fluid entering the patch to exit laterally and a significant feature of the flow is the notable lateral flow diversion within the vegetation patch. This indicates that the lateral channeling effect of the current vegetation distribution is significant. However, when δz increases to 3.125, the larger lateral gap allows more fluid to pass through. Despite the relatively large δx value, few streamlines cross more than two rows of stems. Larger δx and δz promote streamwise flow within the vegetation patch, while smaller δz inhibits it, favoring lateral flow. As δz increases to 4.6875, the lateral movement of the fluid within the vegetation patch further decreases.

Fig. 16 Streamlines through and around the vegetated patch at $\delta x = 3.125$ for different δz , (a1-a2) $\delta z = 1.5625$, (b1-b2) $\delta z = 3.125$, (c1-c2) $\delta z = 4.6875$.

 Based on the side view, it can be observed that as the δx increases, the streamlines become more horizontal. At $\delta x = 1.5625$, the flow entering the vegetation patch from upstream tends to exit from the sides of the patch. However, when δx increases to 4.6875, the interactions between the wakes of the stems weaken, which is due to the spacing between stems is large enough (<u>Chang et al., 2015</u>). The increased spacing allows the flow to pass through, leading to a more orderly downstream flow. The flow entering the first row of stems exits through the gaps in the last row.

Fig. 17 illustrates the vertical vorticity contours and corresponding FFT analysis at $\delta z = 3.125$ for the planes Y = 0.05m, comparing the stem distributions within different regions of vegetation patches. In the case of B2I, where the stem-to-stem spacing in the first three rows is 0.02m, no vortex shedding is observed from the first two rows of stems. However, vortex swing begins from the third row as the shear layers from the first three rows merge. Due to the increased spacing of 0.04m between the third and fourth rows of stems, wave-like wakes are formed downstream. At the downstream of this row, independent shear layers and wave-like wakes develop for the downstream stems. Vortices generated upstream impact the downstream stems, and alternating vortex shedding occurs behind the final row of stems. In the B2 case, the streamwise spacing δx is uniform at 3.125, resulting in shear layers around each stem, with the vortices impacting the downstream stems. The behavior in B2D is the reverse of B2I. In the near-ground plane, a significant reduction in vorticity is observed, indicating a decrease in flow velocity due to ground friction, leading to a more uniform and organized flow pattern. The frequency analysis indicates that the three distinct vegetation configurations exhibit analogous dominant vortex shedding frequencies.

Fig. 17 Vertical vorticity contours in instantaneous fields Y = 0.05m (left column) and 0.002m (right column) for (a) B2I, (b) B2, (c) B2D and the fast Fourier transform at $\delta z = 3.125$ and different distributions in x-direction.

Fig. 18 shows the velocity and vorticity contours for different stem arrangements inside the vegetation patch. In the increasing gap (B2I) case, although the δx between the first three rows of stems is small, the relatively large δz allows the fluid to pass through the gaps along the flow direction. Conversely, in the decreasing gap (B2D) case, the upstream stem density is lower, allowing fluid to enter and develop complex vortex structures before encountering the denser downstream stems, preventing the fluid from flowing out sideways from the dense stem region. Analyzing the vorticity contours, it can be observed that the B2D case contains more vortex structures compared to the B2I

case. This is due to the vortices generated by the upstream stems in the B2D configuration.



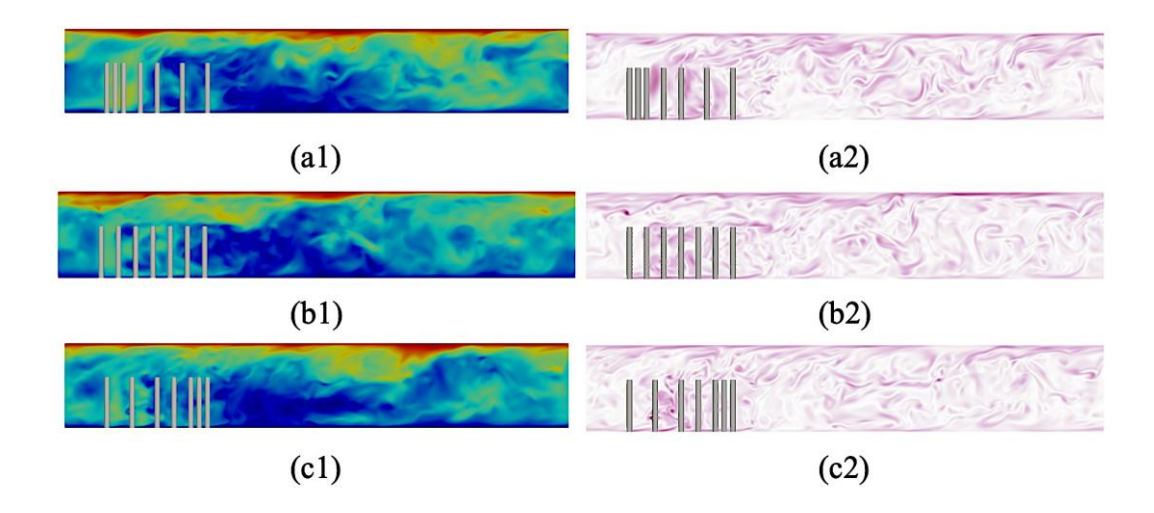


Fig. 18 Velocity (left column) and vorticity (right column) contours in instantaneous fields at Z=0 plane and $\delta z=3.125$ for different distributions in x-direction, (a1-a2) B2I, (b1-b2) B2, (c1-c2) B2D.

Fig. 19 thoroughly illustrates the streamline distribution within the vegetated patches. In the B2I case, the fluid enters the patch with a nearly straight flow initially, experiencing minimal deviation. However, as it moves through the second segment ($\delta x = 3.125$), deviations begin to occur, leading to lateral movements, which intensify in the third segment, resulting in more complex flow patterns. In the B2 case, deviations in the fluid flow occur throughout the patch, with no evidence of rectilinear flow. In the B2D case, the upstream fluid shows significant turbulence, but due to the smaller lateral gaps in the downstream region, the fluid exits in two distinct ways: either from the sides upstream of the dense stem region or by passing through the dense area along the x axis.

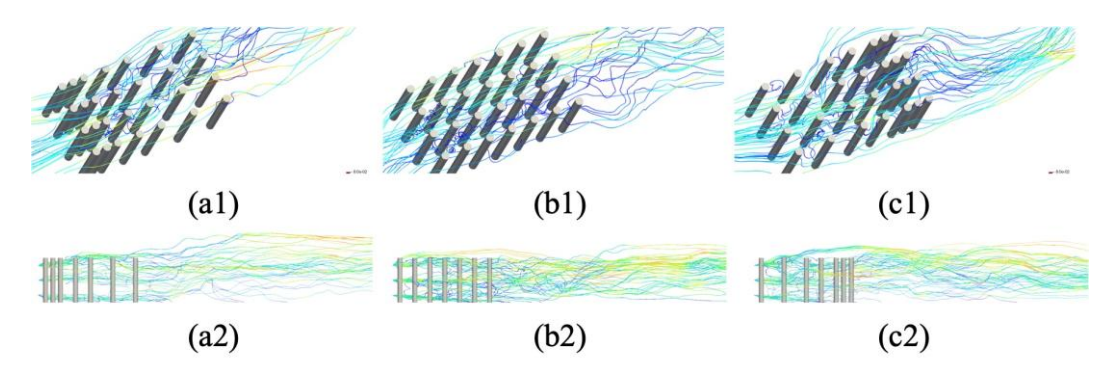


Fig. 19 Streamlines through and around the vegetated patch at $\delta z = 3.125$ for different distributions in x-direction, (a1-a2) B2I, (b1-b2) B2, (c1-c2) B2D.

4.3 Drag coefficient

Fig. 20 shows the drag coefficient (Cd) in the streamwise direction (x-direction) and the lateral force coefficient (Cl) in the spanwise direction (z-direction) on the vegetation patch. The drag and lateral force coefficients can be defined as

$$723 Cd = \frac{\sum_{i} F_d}{0.5\rho WhU_{\infty}^2} (13)$$

$$724 \qquad Cl = \frac{\sum_{i} F_l}{0.5\rho Wh U_{\infty}^2} \tag{14}$$

Fig. 20 Time series of total drag (a) and lateral (b) coefficients of the vegetated patches
 for different δx.

Interestingly, even though the spacing in the z-direction remains constant, altering the streamwise spacing between stems can still significantly impact the drag coefficient. Specifically, when δx increases from 1.5625 or 3.125 to 4.6875, the drag coefficient decreases notably. Regarding the lateral force coefficient, since the vegetated patch is symmetrical about the entire computational domain, the lateral force coefficient oscillates around zero. Moreover, increasing δx significantly reduces the amplitude of these lateral force variations. This reduction is due to the larger gaps between the vegetation patches, which allow more fluid to pass through, thereby reducing the force exerted on the vegetation.

Fig. 21 shows the time series of total drag and lateral force coefficients of the vegetated patches for different δz . It can be seen that as δz increases, Cd decreases. This is because as δz increases, the lateral spacing of the vegetation increases, allowing fluid to pass through the vegetated patches more easily, which reduces the drag experienced by the patches and also decreases the amplitude of the drag variations over time. For Cl, since δx remains constant, the variations in Cl with δz are not significant.

Fig. 22 illustrate the statistical results of the drag coefficient in the vegetation region and the standard deviation of the lift coefficient as functions of the spatial variation parameters δx and δz . The data indicate that the drag and lift in the vegetation area vary significantly with changes in the δx and δz parameters, highlighting the complex hydrodynamic behavior under different geometric conditions. Fig. 22(a) presents the time-averaged drag coefficient. Each bar represents the variation in the drag coefficient of the vegetation region for different combinations of δx and δz . The figure shows a significant change in drag coefficients across different parameter combinations, with the combination of $(\delta x, \delta z) = (3.125, 1.5625)$ resulting in a higher drag coefficient (close to 0.5), while other combinations have lower drag coefficients (around 0.1). This suggests that the drag changes notably as the flow passes around cylinders with varying spacings. Fig. 22(b) depicts the standard deviation of the lift coefficient, reflecting the magnitude of lift fluctuations over time. Higher bars indicate larger fluctuations in the lift coefficient under the combination of $(\delta x, \delta z) = (1.5625, 1.5625)$

3.125), with the standard deviation reaching up to 0.06, while lower bars suggest smaller lift fluctuations. The fluctuation in lift is closely related to the instability of the flow structure and vortex shedding.

Fig. 21 Time series of total drag (a) and lift (b) coefficients of the vegetated patches for different δz .

Fig. 22 The time-averaged drag coefficient (a) and the standard deviation of the lateral coefficient (b) for vegetation patches as a function of variations in δx and δz .

 Fig. 23 illustrates the effect of the streamwise distribution of stems within the vegetated patch on the drag coefficient and lateral force coefficient. It is important to note that the three selected cases have the same length, width, and number of stems within the vegetated patch, differing only in their streamwise distribution. From the drag coefficient figure, it is evident that the B2I case exhibits the highest drag coefficient, followed by the B2 case, with the B2D case showing the lowest drag coefficient. As for the lateral force coefficient, maintaining the overall density of the vegetated patch while altering the internal distribution of the stems does not significantly impact the lateral force coefficient.

Fig. 23 Time series of total drag (a) and lateral (b) coefficients of the vegetated patches with various stems distribution in x-direction.

Conclusion

This study employs Large Eddy Simulation (LES) and Lattice Boltzmann Method (LBM) to investigate flow characteristics through submerged vegetation patches in an open channel. The patch was constructed in alignment with varies spacings. The findings reveal that streamwise (δx) and spanwise (δz) stem spacing critically shape flow dynamics, wake regions, and coherent structures. At δx , $\delta z < 1.5625$, the patch forms a single horseshoe vortex without detached vortices. Increasing δx to 3.125 or 4.6875 generates shear layers, reducing vortex shedding frequency and drag coefficient. Increasing δz to 4.6875 weakens vortex interactions, forming distinct horseshoe vortices and further lowering drag. The non-uniform stem spacing, as exemplified by B2I and B2D, significantly influences flow characteristics, offering preliminary insights for optimizing vegetation layouts. Distribution schemes also affect drag, with coefficients decreasing as $Cd_{B2I} > Cd_{B2} > Cd_{B2D}$, achieving the lowest drag when upstream density is reduced. These results elucidate vegetation-flow interaction

mechanisms, providing a quantitative basis for optimizing open channel design, erosion control, and flood management.

While the current study focuses on three key distribution schemes (B2, B2I, B2D) to establish the influence of stem spacing variation, it is acknowledged that additional patterns, such as random or staggered arrangements, could further broaden the findings. Future work may explore these configurations to enhance the generalizability of the results. Specifically, advanced computational studies incorporating multi-patch configurations and staggered arrangements would be particularly valuable for establishing more comprehensive design guidelines.

Acknowledgement

This project has been supported by the Hong Kong Polytechnic University (projects no. 1-W295 and no. 1-CDLC) and the Hong Kong Research Grants Council (RGC) under project no. C5002-22Y and the NSFC/RGC Joint Research Scheme (JRS) under project no. N PolyU559/22.

815

816817

Notations

 f_i density distribution function τ relaxation time e_i discrete velocity w_i weighting factor

u kinematic viscosity ρ density u velocity u that is a constant u that u is a constant u is a constant u that u is a constant u is a constant u that u is a constant u is a constant u is a constant u is a constant u is a constant

W width of vegetation patch L length of vegetation patch

H water depth Φ averaged solid volume fraction

d diameter of stem dx streamwise spacing dz spanwise spacing

 δx non-dimensional streamwise spacing δz non-dimensional spanwise spacing

Fr Froude number Re channel Reynolds number Cd drag force coefficient Cl lateral force coefficient

References

- 819 Chang K, Constantinescu G. Numerical investigation of flow and turbulence structure
- through and around a circular array of rigid cylinders. Journal of Fluid Mechanics.
- 821 2015 Aug;776:161-99.
- Chen, S., & Doolen, G. D. (1998). Lattice Boltzmann method for fluid flows. Annual review of fluid mechanics, 30(1), 329-364.
- Coratger T, Farag G, Zhao S, Boivin P, Sagaut P. Large-eddy lattice-Boltzmann modeling of transonic flows. Physics of Fluids. 2021 Nov 1;33(11).
- Del Tánago MG, Martínez-Fernández V, Aguiar FC, Bertoldi W, Dufour S, de Jalón DG, Garófano-Gómez V, Mandzukovski D, Rodríguez-González PM. Improving river hydromorphological assessment through better integration of riparian vegetation: Scientific evidence and guidelines. Journal of Environmental
- 830 Management. 2021 Aug 15;292:112730.
- Dubief Y, Delcayre F. On coherent-vortex identification in turbulence. Journal of turbulence. 2000 Dec 1;1(1):011.
- Edwards PJ, Kollmann J, Gurnell AM, Petts GE, Tockner K, Ward JV. A conceptual model of vegetation dynamics on gravel bars of a large Alpine river. Wetlands Ecology and Management. 1999 Sep;7:141-53.
- Etminan V, Lowe RJ, Ghisalberti M. A new model for predicting the drag exerted by vegetation canopies. Water Resources Research. 2017 Apr;53(4):3179-96.
- Frederich O, Wassen E, Thiele F, Jensch M, Brede M, Hüttmann F, Leder A. Numerical simulation of the flow around a finite cylinder with ground plate in comparison to experimental measurements. InNew Results in Numerical and Experimental Fluid Mechanics VI: Contributions to the 15th STAB/DGLR Symposium Darmstadt,
- Germany, 2008 (pp. 348-355). Springer Berlin Heidelberg.
- Fu HS, Wang D, Li WQ, Ren BL, Yang KJ. Velocity and turbulence characteristics in an open channel with multi-row staggered vegetation patches. Journal of Hydrodynamics. 2021 Oct;33(5):1035-44.
- 846 Guo, Z., & Shu, C. (2013). Lattice Boltzmann method and its application in engineering (Vol. 3). World Scientific.
- Li D, Huai W, Guo Y, Liu M. Flow characteristics in partially vegetated channel with homogeneous and heterogeneous layouts. Environmental Science and Pollution Research. 2022 May;29(25):38186-97.
- Li D, Liu M, Huai W, Liu G, Peng Z, Zhang F. Conditional statistics of Reynolds stress in open channel flows with modeled canopies of homogeneous and heterogeneous density. Physics of Fluids. 2023 Mar 1;35(3).
- Liu C, Nepf H. Sediment deposition within and around a finite patch of model vegetation over a range of channel velocity. Water Resources Research. 2016 Jan;52(1):600-12.

- Liu H, Liu M, Ai Y, Huai W. Turbulence characteristics in partially vegetated open
- channels with alternating sparse and dense patches. Physics of Fluids. 2024 Jan 1;36(1).
- Liu M, Huai W, Ji B. Characteristics of the flow structures through and around a submerged canopy patch. Physics of Fluids. 2021 Mar 1;33(3).
- Liu M, Huai W, Ji B. Characteristics of the flow structures through and around a submerged canopy patch. Physics of Fluids. 2021 Mar 1;33(3).
- Liu M, Yang Z, Ji B, Huai W, Tang H. Flow dynamics in lateral vegetation cavities constructed by an array of emergent vegetation patches along the open-channel bank. Physics of Fluids. 2022 Mar 1;34(3).
- Malaspinas O, Sagaut P. Advanced large-eddy simulation for lattice Boltzmann methods: The approximate deconvolution model. Physics of Fluids. 2011 Oct 1;23(10).
- Nakayama K, Shintani T, Komai K, Nakagawa Y, Tsai JW, Sasaki D, Tada K, Moki H, Kuwae T, Watanabe K, Hipsey MR. Integration of submerged aquatic vegetation motion within hydrodynamic models. Water Resources Research. 2020 Aug;56(8):e2020WR027369.
- Nandi KK, Kakati R, Dutta S, Khatua KK. Exploring the Influence of Vegetated Mid-Channel Bar on Flow and Turbulence in Bifurcated Channels: An Experimental Approach. Advances in Water Resources. 2024 May 22:104727.
- Nepf HM. Flow and transport in regions with aquatic vegetation. Annual review of fluid mechanics. 2012 Jan 21;44:123-42.
- Siodlaczek M, Gaedtke M, Simonis S, Schweiker M, Homma N, Krause MJ. Numerical evaluation of thermal comfort using a large eddy lattice Boltzmann method. Building and Environment. 2021 Apr 1;192:107618.
- Smagorinsky J. General circulation experiments with the primitive equations: I. The basic experiment. Monthly weather review. 1963 Mar 1;91(3):99-164.
- 884 Son O, Gao AK, Gursul I, Cantwell Cd, Wang Z, Sherwin SJ. Leading-edge vortex 885 dynamics on plunging airfoils and wings. Journal of Fluid Mechanics. 2022 886 Jun;940:A28.
- Sumner D. Flow above the free end of a surface-mounted finite-height circular cylinder:
 A review. Journal of Fluids and Structures. 2013 Nov 1;43:41-63.
- Wang M, Avital E, Chen Q, Williams J, Mi S, Xie Q. A numerical study on suspended sediment transport in a partially vegetated channel flow. Journal of Hydrology. 2021 Aug 1;599:126335.
- Waterman BR, Hansen AT. Hydro biogeochemical controls on nitrate removal: Insights from artificial emergent vegetation experiments in a recirculating flume mesocosm. Water Resources Research. 2024 Aug;60(8):e2023WR036995.
- Wu F, Yin Z, Wang Y, Jiang X. Numerical investigation of the restored oyster reef flow field with the lattice Boltzmann method. Physics of Fluids. 2024 Apr 1;36(4).

- Yagci O, Strom K. Reach-scale experiments on deposition process in vegetated channel:

 Suspended sediment capturing ability and backwater effect of instream plants.
- Journal of Hydrology. 2022 May 1;608:127612.

- Yamasaki TN, de Lima PH, Silva DF, Preza CG, Janzen JG, Nepf HM. From patch to
 channel scale: The evolution of emergent vegetation in a channel. Advances in
 Water Resources. 2019 Jul 1;129:131-45.
- 903 Yu ZJ, Shan YQ, Liu C, Liu XN. Wake flow and vortex structures behind emergent 904 vegetation patches elongated in the longitudinal direction. Journal of 905 Hydrodynamics. 2021 Dec;33(6):1148-61.
- Zhang J, Zhang S, Wang C, Wang W, Ma L. Flow characteristics of open channels based
 on patch distribution of partially discontinuous rigid combined vegetation.
 Frontiers in Plant Science. 2022 Oct 11;13:976646.
- Zhang Y, Lai X, Zhang L, Song K, Yao X, Gu L, Pang C. The influence of aquatic
 vegetation on flow structure and sediment deposition: A field study in Dongting
 Lake, China. Journal of Hydrology. 2020 May 1;584:124644.
- Zhang YH, Duan HF, Yan XF, Stocchino A. Experimental study on the combined effects
 of patch density and elongation on wake structure behind a rectangular porous
 patch. Journal of Fluid Mechanics. 2023 Mar;959:A36.
- Zong L, Nepf H. Spatial distribution of deposition within a patch of vegetation. Water
 Resources Research. 2011 Mar;47(3).